J Strain Analysis
XX(X):1–27

DOI: 10.1177/ToBeAssigned
www.sagepub.com/
SAGE

Evaluation of heterogeneous mechanical tests for model calibration of sheet metals

M.G. Oliveira[1,2], S. Thuillier[2], A. Andrade-Campos[1]

Abstract

The accuracy of strategies combining heterogeneous mechanical tests and full-field strain measurement techniques is dependent on many factors. Recently, many heterogeneous mechanical tests with different specimen shapes have been proposed using optimization techniques or empirical knowledge. However, a comparison of heterogeneous mechanical tests is a difficult task because studies use different materials and different representations of the strain and stress states. This work discusses metrics, calculated from the stress and strain tensors, to evaluate heterogeneous mechanical tests and proposes a metric to evaluate the tests' sensitivity to anisotropy. To illustrate the approach, four heterogeneous mechanical tests are evaluated through the use of the suggested metrics. Results show that the use of various metrics provide a good basis to evaluate heterogeneous mechanical tests. Moreover, this work identifies a heterogeneous mechanical test achieving a high range of mechanical states and high values of equivalent plastic strain.

Keywords

heterogeneous mechanical tests, sheet metals, material behaviour characterisation, plasticity, anisotropy

[1]Centre for Mechanical Technology and Automation (TEMA), Department of Mechanical Engineering, University of Aveiro, 3810-193 Aveiro, Portugal
[2]Univ. Bretagne Sud, UMR CNRS 6027, IRDL, F-56100 Lorient, France

Corresponding author:
M.G Oliveira, Centre for Mechanical Technology and Automation (TEMA), Department of Mechanical Engineering, University of Aveiro, 3810-193 Aveiro, Portugal
Email: oliveiramiguel@ua.pt

Prepared using sagej.cls *[Version: 2017/01/17 v1.20]*

Introduction

The mechanical design of sheet metal forming parts tends to be more virtual, decreasing associated delays and manufacturing processes costs. Consequently, materials' mechanical characterisation has received increased attention due to the need for accurate input data to computational analysis software.

The materials' mechanical behaviour can be numerically described through constitutive models, which can be calibrated using standard quasi-homogeneous mechanical tests[1]. Nevertheless, from a single classical mechanical test, it is difficult to extract many material parameters, requiring several tests to identify many material parameters of a single constitutive model[2,3].

More recently, research has focused on alternative methods based on mechanical tests inducing heterogeneous strain fields, measured through full-field experimental techniques, providing significantly more valuable data[4–6]. Ideally, a single mechanical test should be enough to characterise the material's mechanical behaviour. However, the accuracy of these alternative methods depends on several factors: (i) the applied load and shape of the specimen used in the mechanical test[7]; (ii) the choice of an appropriate strain field measurement technique[8]; or (iii) the definition of an identification strategy[9]. Indeed, the heterogeneity does not lead to any analytical post-treatment and a suitable inverse identification technique, such as the finite element model updating method[10] or the virtual fields method[11,12].

Although many challenges still exist in this field, selecting and designing the most suitable heterogeneous mechanical tests for sheet metals' constitutive model calibration is still a topic under research. In recent times, the design of novel heterogeneous mechanical tests using different strategies has increased. An innovative approach adopted a shape optimisation procedure to design a butterfly-shaped specimen under uniaxial tensile loading[13,14]. A different approach analysed configurations of notched specimens by evaluating the error between synthetic images and numerical simulations[15]. More recently, some studies used topology optimisation, allowing more flexibility in the design process and resulting in complex geometries. Another work proposed a bridge-like specimen based on the plate buckling theory[16]. The bridge-like specimen is the first attempt to design a heterogeneous mechanical test that can characterise sheet metals' mechanical behaviour under cyclic loadings.

Generally, the quality and quantity of heterogeneous mechanical tests have increased. However, a qualitative or quantitative comparison is not straightforward because studies use different materials and representations of output data. To solve this problem, Souto et al.[17] proposed a quantitative indicator to evaluate and classify mechanical tests. The indicator evaluates the mechanical test up to rupture and is based on the strain heterogeneity. Although this methodology is considered innovative, it was material-dependent and did not consider the tests' sensitivity to material anisotropy[18]. Additionally, heterogeneous mechanical tests' sensitivity to material parameters is a relevant metric to evaluate the tests' richness[17]. In this scope, Hapsari et al.[19] used an indicator that quantifies the identifiability of a parameters' subset based on the largest and smallest eigenvalue of the dimensionless sensitivity matrix. Nonetheless,

this methodology depends highly on the constitutive model and can be computationally expensive.

This work proposes metrics based on the strain and stress states, to fill the existing gap in evaluating heterogeneous mechanical tests. A metric is proposed to evaluate the tests' sensitivity to anisotropy, named rotation angle. Within a numerical approach, four heterogeneous mechanical tests and three materials are evaluated.

The paper is organised into six sections. The following section introduces the materials and constitutive model's formulation. Afterwards, the heterogeneous mechanical tests and numerical considerations on the finite element analyses are presented. Then, the proposed metrics are presented, and finally, the heterogeneous mechanical tests' evaluation is discussed. Lastly, conclusions and future remarks are outlined.

Numerical characterisation of materials

This section starts by introducing the constitutive model used to represent the materials' mechanical behaviour. Afterwards, three materials are introduced. These materials are virtual, but their parameters are identified from real experiments. For simplicity's sake, the materials are virtually represented using the same constitutive model. Dealing with sheet metals, a plane stress state formulation is chosen. Lastly, the condition used to represent the maximum deformation each material can sustain is introduced.

Constitutive model

An elastoplastic constitutive model for an anisotropic material is composed of an anisotropic yield criterion and a hardening law, either isotropic or mixed, with the latter generally used to characterise reverse loadings. Because this work only considers monotonic loadings, an isotropic hardening law is adopted. Also, it is expected that the calibration of a constitutive model is based on mechanical information under distinct strain paths and material orientations, defined by three orthotropic axes: rolling direction (RD), transverse direction (TD), and normal direction (ND).

The same constitutive model describes the elastoplastic behaviour of the materials. Its formulation assumes the additive composition of the strain rate tensor and an associated flow rule. The elastic behaviour is isotropic, described by Hooke's law, and the plastic behaviour is anisotropic.

In plasticity, the yield condition $f\left(\boldsymbol{\sigma}, \bar{\varepsilon}^{\mathrm{p}}\right)$, assuming isotropic hardening, can be expressed as

$$f\left(\boldsymbol{\sigma}, \bar{\varepsilon}^{\mathrm{p}}\right) = \bar{\sigma}(\boldsymbol{\sigma}) - \sigma_{\mathrm{y}}(\bar{\varepsilon}^{\mathrm{p}}) = 0, \tag{1}$$

where $\bar{\sigma}(\boldsymbol{\sigma})$ is the equivalent stress as a function of the stress tensor $\boldsymbol{\sigma}$ and $\sigma_{\mathrm{y}}(\bar{\varepsilon}^{\mathrm{p}})$ is the yield stress as a function of the equivalent plastic strain $\bar{\varepsilon}^{\mathrm{p}}$. The Swift's law describes the isotropic hardening and is written as

$$\sigma_{\mathrm{y}}(\bar{\varepsilon}^{\mathrm{p}}) = K(\varepsilon_0 + \bar{\varepsilon}^{\mathrm{p}})^n, \text{ with} \tag{2}$$

$$\varepsilon_0 = \left(\frac{\sigma_0}{K}\right)^{1/n}, \tag{3}$$

where K is the strength coefficient; ε_0 is the initial yield strain; n is the strain-hardening exponent; and σ_0 is the initial yield stress. The Yld2000-2d anisotropic yield criterion describes the yield surface[20] and is expressed as

$$2\bar{\sigma}^a = \left|X'_1 - X'_2\right|^a + \left|2X''_2 + X''_1\right|^a + \left|2X''_1 + X''_2\right|^a, \tag{4}$$

where a is a material-dependent parameter, usually, assuming the values of 6 or 8. X'_i and X''_i $(i = 1, 2)$ are the eigenvalues of the tensors $\mathbf{X}'$ and $\mathbf{X}''$ obtained after two linear transformations on the stress tensor. These transformations can be directly determined from the stress tensor $\boldsymbol{\sigma}$ as

$$\mathbf{X}' = \mathbf{L}' : \boldsymbol{\sigma}, \tag{5}$$

$$\mathbf{X}'' = \mathbf{L}'' : \boldsymbol{\sigma}, \tag{6}$$

where ":" denotes the contracted product between two tensors, and the linear transformation tensors $\mathbf{L}'$ and $\mathbf{L}''$ are defined as

$$\mathbf{L}' = \begin{bmatrix} L'_{11} \\ L'_{12} \\ L'_{21} \\ L'_{22} \\ L'_{66} \end{bmatrix} = \frac{1}{3} \begin{bmatrix} 2 & 0 & 0 \\ -1 & 0 & 0 \\ 0 & -1 & 0 \\ 0 & 2 & 0 \\ 0 & 0 & 3 \end{bmatrix} \begin{bmatrix} \alpha_1 \\ \alpha_2 \\ \alpha_7 \end{bmatrix}, \tag{7}$$

$$\mathbf{L}'' = \begin{bmatrix} L''_{11} \\ L''_{12} \\ L''_{21} \\ L''_{22} \\ L''_{66} \end{bmatrix} = \frac{1}{9} \begin{bmatrix} -2 & 2 & 2 & -2 & 0 \\ 1 & -4 & -4 & 4 & 0 \\ 4 & -4 & -4 & 1 & 0 \\ -2 & 8 & 2 & -2 & 0 \\ 0 & 0 & 0 & 0 & 0 \end{bmatrix} \begin{bmatrix} \alpha_3 \\ \alpha_4 \\ \alpha_5 \\ \alpha_6 \\ \alpha_8 \end{bmatrix}, \tag{8}$$

where α_k $(k = 1, ..., 8)$ are the anisotropy coefficients representing the material-dependent parameters.

Materials

The analysis considers three sheet metals, to account for the heterogeneous mechanical tests' sensitivity to different materials: (i) an aluminium alloy (AA2090-T3) with a nominal thickness of $1.6\,\text{mm}$[21–23]; (ii) a dual-phase steel (DP600) with a nominal thickness of $0.8\,\text{mm}$[24]; and (iii) a cold-rolled sheet of 99.9% pure copper (Cu) with a nominal thickness of $0.1\,\text{mm}$[25,26].

The elastic properties of the materials (Young's modulus E and Poisson's ratio ν), and the parameters of Yld2000-2d anisotropic yield criterion and Swift's isotropic hardening law are provided in Table 1. The pure copper parameters were obtained through an identification process[1], where a good agreement between experimental and numerical

data was obtained. It is worth highlighting that the model calibrations used in this study come from experimental data and therefore provide a realistic mechanical behaviour to the virtual materials up to a certain strain level. Additionally, the same phenomenological model is used for all materials for a straightforward and fast comparison.

Concerning the material's mechanical behaviour, DP600 is characterised by a much higher initial yield stress than AA2090-T3 and Cu, while the latter presents a much lower hardening rate than the former (see Fig. 1). Moreover, Figs. 2a and 2b present the normalised yield stress and the Lankford coefficient for various tensile orientations. These representations show the considerable variation of both normalised yield stress and Lankford coefficient of AA2090-T3 compared to Cu and DP600. Besides, the latter exhibits, on average, values close to 1 in both representations, whereas the Lankford coefficients of Cu are below 1, representing a relatively high normal anisotropy. The yield surface's projection on the planes of normalised RD-TD and shear-RD stress also highlights the anisotropic behaviour, respectively, represented in Figs. 2c and 2d.

Table 1. Material's elastic properties and parameters used in Yld2000-2d anisotropic yield criterion and Swift's isotropic hardening law, for AA2090-T3[21,22], DP600[24], and Cu[26].

Model	Parameter	AA2090-T3	DP600	Cu	Unit
Elastic	E	69	210	104	GPa
	ν	0.33	0.30	0.28	-
Yld2000-2d	α_1	0.860	1.011	0.893	-
	α_2	0.929	0.964	1.013	-
	α_3	0.957	1.191	0.644	-
	α_4	0.977	0.995	0.985	-
	α_5	1.063	1.010	0.981	-
	α_6	1.039	1.018	0.857	-
	α_7	−1.251	0.977	0.958	-
	α_8	1.450	0.935	1.322	-
	a	8	6	8	-
Swift	σ_0	279.6	355.1	240.2	MPa
	K	646.0	979.5	350.8	MPa
	n	0.227	0.194	0.129	-

Forming limit curves

In evaluating heterogeneous mechanical tests, it is relevant to consider the maximum deformation the material can sustain relative to a specific condition. This condition can be, among others, the maximum equivalent plastic strain, a rupture criterion or a forming limit curve (FLC). The latter is a feature of the forming limit diagram (FLD), typically used to evaluate the formability of sheet metals[27]. The FLC corresponds to the strain limits the material can sustain at the onset of necking. In the regions above the FLC, necking or deformation instability may occur, and below represents the safe forming regions.

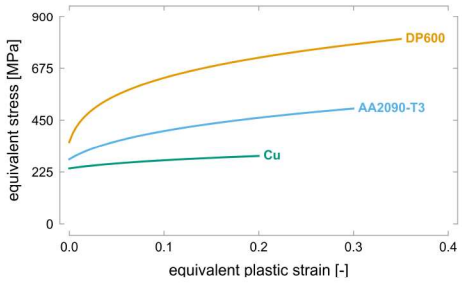

Figure 1. Virtual representation of AA2090-T3, DP600, and Cu's strain-hardening behaviour.

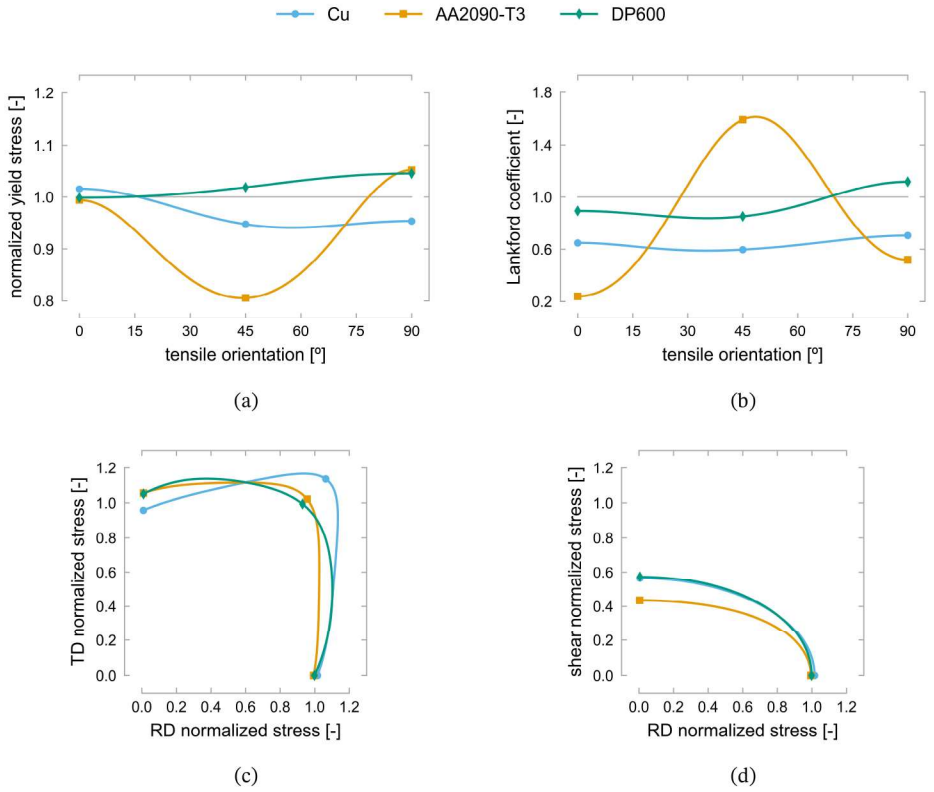

Figure 2. Virtual representations of AA2090-T3, DP600, and Cu's anisotropic behaviour: (a) anisotropy of normalized yield stress along tensile orientations between $0°$ and $90°$ from the RD; (b) anisotropy of Lankford coefficient along tensile orientations between $0°$ and $90°$ from the RD; (c) projection of initial yield surface on the plane of RD-TD normalized stress; and (d) projection of initial yield surface on the plane of shear-RD normalized stress.

With the purpose of a fair comparison between the heterogeneous mechanical tests, an FLC is virtually generated for each material. The adopted shape is a simplified version of real FLCs, but based on typical FLCs and the material's strain-hardening exponent n (see Table 1) for the maximum value in the plane strain tension region ($\varepsilon_2/\varepsilon_1 = 0$)[28], with ε_1 and ε_2, respectively, the major and minor strain. Moreover, the virtually generated FLCs are characterised by a slope of -1.0 (left-hand side) and 0.5 (right-hand side), as presented in Fig. 3. Reference data is also added in Fig. 3 for comparison with the virtually generated FLCs[23–25]. Although not exact, the virtually generated FLCs are correct approximations of the reference data. Considering that the analysis is limited to monotonic loadings, a material point A is expected to present a linear strain path. Thus, if at time increment t the material point A_t is located at a given position in the FLD, the strain path is linear and the material point is expected to reach the FLC at A_∞. However, the purpose of using the FLC here is simply to know when it is reached. By numerically evaluating the vertical distance (evaluated on the major strain axis, for the same value of minor strain) from the material point A_t to the FLC, represented by the point B_t, it is possible to identify when the limit is reached. Consequently, this distance, represented by W_{FLC}, is numerically evaluated as

$$W_{\mathrm{FLC}} = \frac{\varepsilon_1^{\mathrm{A}_t}}{\varepsilon_1^{\mathrm{B}_t}}, \tag{9}$$

where $\varepsilon_1^{\mathrm{A}_t}$ and $\varepsilon_1^{\mathrm{B}_t}$ are, respectively, the major in-plane principal strain at the material point A_t and at the corresponding point B_t on the FLC (see Fig. 3). Whenever the condition $W_{\mathrm{FLC}} > 1$ is satisfied, the forming limit is reached and the test stops.

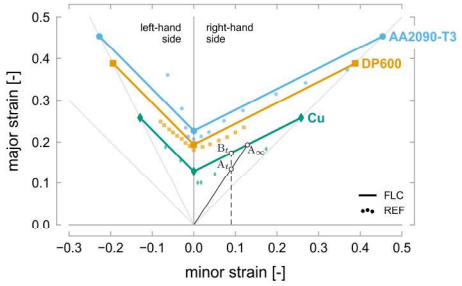

Figure 3. Virtual forming limit curves of AA2090-T3, DP600, and Cu. The virtual forming limit curves (FLC) are characterized by the material's strain-hardening exponent in the plane strain tension region, and by a slope of -1.0 on the left-hand side and 0.5 on the right-hand side of the diagram. Reference data (REF) from the literature is also represented for each material[23–25]. The position in the diagram of a material point A at time increment t is represented by A_t, and A_∞ is the position of A when it reaches the forming limit curve on a linear strain path. Point B_t represents the position used to evaluate the vertical distance from the material point A_t to the forming limit curve.

Heterogeneous mechanical tests and numerical models

This section introduces the four heterogeneous mechanical tests analysed, proposed to maximise the strain field heterogeneity. The tests are modelled using symmetry conditions to reduce the numerical simulations' computational cost, and the loading is displacement driven. The tests, named Test A, Test B, Test C, and Test D, and finite element models' boundary conditions are described. Lastly, this section introduces numerical considerations of the finite element analyses.

Test A is a biaxial tensile test with a centred hole, designed to generate a heterogeneous strain field (see Fig. 4a)[29]. The authors considered that the test could reach a deformation able to properly calibrate the hardening behaviour while depending on the rolling direction to calibrate the anisotropic behaviour. Moreover, the range of stress states achieved was between uniaxial and equibiaxial tension. The numerical model uses symmetry conditions in the rolling and transverse directions, by default, aligned with the loading directions (see Fig. 4a).

Test B was designed as a hybrid shape between a classical tensile test and a plane strain tensile test (see Fig. 4b)[30]. The shape's interest was investigated by comparing it with standard mechanical tests and evaluating the strain field's heterogeneity and sensitivity to material parameters. Additionally, the analysis accounted for some limitations of the digital image correlation system: regions near the free edges and strain levels below digital image correlation accuracy. This study concluded that the new heterogeneous mechanical test performed better than standard mechanical tests in all of the criteria. The numerical model uses symmetry conditions in the rolling and transverse directions, with the rolling and loading directions aligned (see Fig. 4b).

Test C is a uniaxial tensile test, designed from empirical knowledge and trial and error, resulting in a geometry resembling a Greek capital letter sigma Σ (see Fig. 4c)[31]. The authors showed that this test exhibits various stress states. Also, combining two tests loaded in different material orientations, increased the mechanical information and improved the calibration. Test C is numerically modelled using one symmetry condition in the rolling direction, by default, aligned with the loading direction (see Fig. 4c).

Test D is a uniaxial tensile test, designed via an iterative process of finite element analyses (see Fig. 4d)[32]. The process started with a shape based on empirical knowledge, then manually adjusted to meet several criteria, such as maximising stress heterogeneity and minimising large gradients in strain near free edges. The optimised geometry resembles a capital letter "D", and the authors showed that it could cover a reasonable extent of stress states. Similarly to Test C, one symmetry condition in the rolling direction is used in the numerical model of Test D, and the rolling direction is also aligned with the loading direction (see Fig. 4d).

The numerical models are two-dimensional, assuming a plane stress state formulation. A four-node bilinear plane stress element, with reduced integration and stiffness hourglass control, is used, as well as a large strain formulation. A very refined mesh with a maximum element size of 0.1 mm is used, to obtain many material points approaching a continuous state of the material. Furthermore, to account for the limitations of a subset-based digital image correlation system, which does not provide information near

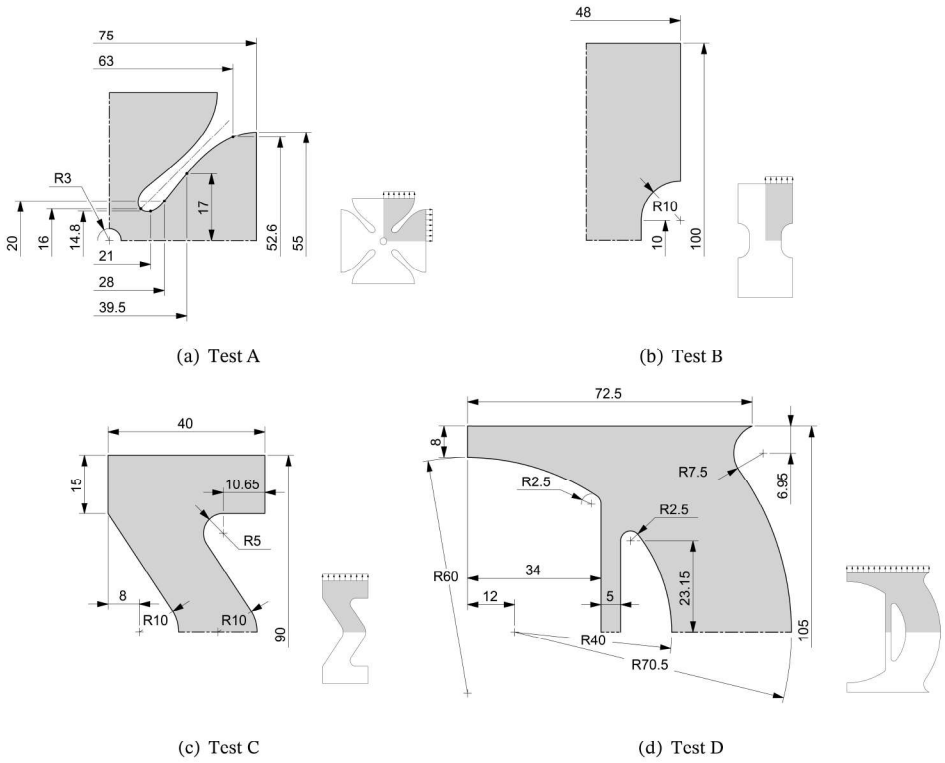

Figure 4. Geometry (dimensions in mm) and boundary conditions of the finite element models for the heterogeneous mechanical tests: (a) Test A, (b) Test B, (c) Test C, and (d) Test D. The geometry of the specimen is represented using symmetries and the presented values correspond to the measurement's total dimension. The small drawing on the right-hand side recalls the full geometry and the loading directions.

the specimen's free edges, the results are analysed for a region of interest, defined by an arbitrary boundary of 0.25 mm on the free edges of the specimen. Finally, the numerical simulations are performed with automatic time stepping, maximum increment size of 0.01, and the constitutive model is implemented using a user-defined material subroutine[33].

Metrics to analyse strain and stress states

As many heterogeneous mechanical tests already exist, selecting the best one is not a straightforward task. To aid in the decision or design process, authors tend to use standard metrics to evaluate the tests' richness. This section presents the five metrics selected to evaluate heterogeneous mechanical tests: the equivalent plastic strain; the major and minor strain; the major and minor stress; the stress triaxiality and Lode angle parameter;

and the rotation angle. For simplicity's sake, each metric already assumes a plane stress state formulation.

Equivalent plastic strain

The equivalent plastic strain $\bar{\varepsilon}^{\mathrm{p}}$ is a metric that quantifies the level of plastic strain reached during the tests and is given by

$$\bar{\varepsilon}^{\mathrm{p}} = \int_0^t \dot{\bar{\varepsilon}}^{\mathrm{p}} \mathrm{d}t, \tag{10}$$

where $\dot{\bar{\varepsilon}}^{\mathrm{p}}$ is the rate of equivalent plastic strain. This metric is relevant for metallic materials and within the context of sheet metal forming. Indeed, if more data is available for higher equivalent plastic strain levels, the calibration accuracy is expected to improve. Concerning heterogeneous mechanical tests, it is beneficial to achieve high equivalent plastic strain levels in many regions. This way, the equivalent plastic strain can also be used as a measure of the tests' heterogeneity, where a large region of the test presenting high levels of strain is desired, as opposed to observing strain localisation in a reduced region.

Major and minor strain

The major and minor strain, respectively, ε_1 and ε_2, with $\varepsilon_1 > \varepsilon_2$, are the principal values of the strain tensor $\boldsymbol{\varepsilon}$ calculated on the sheet plane as

$$\varepsilon_{1,2} = \frac{\varepsilon_{\mathrm{xx}} + \varepsilon_{\mathrm{yy}}}{2} \pm \sqrt{\left(\frac{\varepsilon_{\mathrm{xx}} - \varepsilon_{\mathrm{yy}}}{2}\right)^2 + \varepsilon_{\mathrm{xy}}^2}, \tag{11}$$

where $\varepsilon_{\mathrm{xx}}$, $\varepsilon_{\mathrm{yy}}$, and $\varepsilon_{\mathrm{xy}}$ are the strain tensor's components in the material frame, with x and y denoting, respectively, the rolling and transverse directions on the sheet plane.

The combination of major and minor strain values can characterise the mechanical state, denoted as strain state. This metric analysis is typically presented using the major and minor strain diagram, as shown in Fig. 5a. Then, as reference values of $\varepsilon_2/\varepsilon_1$ define typical mechanical states for an isotropic material (such as $\varepsilon_2/\varepsilon_1 = -0.5$ defining uniaxial tension and shear by $\varepsilon_2/\varepsilon_1 = -1$, as listed in Table 2), the diagram identifies the strain states achieved. The major and minor strain diagram is also known as the forming limit diagram.

Moreover, the major and minor strain is relevant to infer the diversity of strain states achieved. A primary characteristic of using the major and minor strain to evaluate heterogeneous mechanical tests is that it can be experimentally measured.

Major and minor stress

The major and minor stress, σ_1 and σ_2, with $\sigma_1 > \sigma_2$, are the principal values of the stress tensor $\boldsymbol{\sigma}$ calculated on the sheet plane as

$$\sigma_{1,2} = \frac{\sigma_{xx} + \sigma_{yy}}{2} \pm \sqrt{\left(\frac{\sigma_{xx} - \sigma_{yy}}{2}\right)^2 + \sigma_{xy}^2}, \tag{12}$$

where σ_{xx}, σ_{yy}, and σ_{xy} are the stress tensor's components in the material frame.

Analogously to the major and minor strain, the mechanical state analysed through the stress tensor represents the stress state. This analysis is typically presented using the major and minor stress diagram, as shown in Fig. 5b. Similarly to the major and minor strain, reference values of σ_2/σ_1 represent typical mechanical states (such as uniaxial tension represented by $\sigma_2/\sigma_1 = 0$ and shear by $\sigma_2/\sigma_1 = -1$, as listed in Table 2).

These last two metrics are commonly used to evaluate mechanical states' distribution, either through a strain- or stress-based representation. Because the strain fields are obtained from experiments, a strain-based representation is usually associated with experimental data. On the other hand, a stress-based representation is associated with numerical data[16,31,32,34–37]. Studies considering both representations are limited[18,29].

Stress triaxiality and Lode angle parameter

The stress triaxiality and the Lode angle parameter are two dimensionless indicators that can characterise a mechanical state. Both represent the stress tensor $\boldsymbol{\sigma}$, through stress invariants, and have been used in works related to ductile fracture[38–40]. Nonetheless, their interest in evaluating the richness of heterogeneous mechanical tests has not yet been investigated. The stress triaxiality η represents the distribution of stress in the three orthotropic directions and can be given by

$$\eta = \frac{\sigma_h}{\bar{\sigma}_{VM}} = \frac{(\sigma_{xx} + \sigma_{yy})/3}{\sqrt{\sigma_{xx}^2 + \sigma_{yy}^2 - \sigma_{xx}\sigma_{yy} + 3\sigma_{xy}^2}}, \tag{13}$$

where σ_h is the hydrostatic stress, and $\bar{\sigma}_{VM}$ is the von Mises equivalent stress. The range of stress triaxiality values is $-\infty < \eta < +\infty$; however, in the case of plane stress state, the range is reduced to $-2/3 \leq \eta \leq 2/3$. Additionally, stress triaxiality values of $\eta > 0$ characterise tensile states, and of $\eta < 0$ characterise compressive states.

The Lode angle θ, or the Lode parameter L, relates to the third invariant of the deviatoric stress tensor J_3 normalised by the von Mises equivalent stress $\bar{\sigma}_{VM}$, through

$$L = -\cos(3\theta) = -\left(\frac{J_3}{\bar{\sigma}_{VM}}\right)^3, \tag{14}$$

where J_3 is given by

$$J_3 = -\frac{1}{27}(\sigma_{xx} - 2\sigma_{yy})(\sigma_{yy} - 2\sigma_{xx})(\sigma_{xx} + \sigma_{yy}). \tag{15}$$

The range of the Lode angle is $0 \leq \theta \leq \pi/3$, and the Lode parameter's range is $-1 \leq L \leq 1$. Additionally, the Lode angle θ can be normalized as

$$\bar{\theta} = 1 - \frac{2}{\pi} \arccos\left(\frac{J_3}{\bar{\sigma}_{\mathrm{VM}}}\right)^3. \tag{16}$$

where $\bar{\theta}$ is the Lode angle parameter of range $-1 \leq \theta \leq 1$.

Similarly to the two previous metrics, reference values of η and $\bar{\theta}$ represent typical mechanical states, such as uniaxial tension by $\eta = 1/3$ and $\bar{\theta} = 1$ and shear by $\eta = \bar{\theta} = 0$ (see Figure 5 and Table 2).

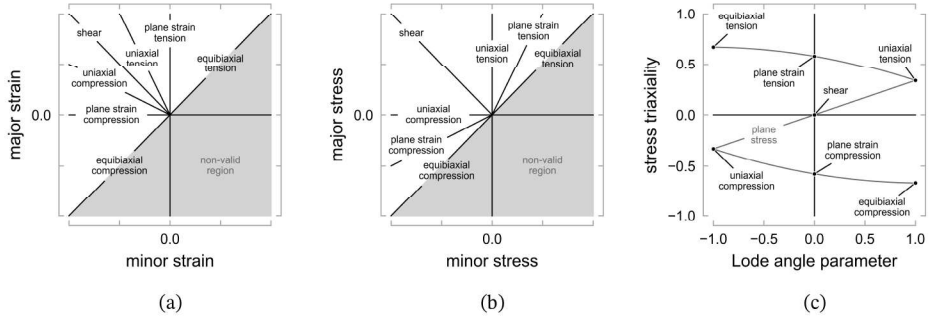

Figure 5. An overview of mechanical states, for an isotropic material and plane stress state, represented through the diagrams of: (a) major and minor strain, (b) major and minor stress, and (c) stress triaxiality and Lode angle parameter.

Rotation angle

A metric able to evaluate the test's sensitivity to anisotropy has not yet been fully explored to evaluate heterogeneous mechanical tests. A possible representation for this behaviour is based on the principal angle between the principal stress base and the material orthotropic axes. The formulation is derived from Mohr's circle equations for a plane stress state and is given by

$$\tan 2\beta = \frac{2\sigma_{\mathrm{xy}}}{\sigma_{\mathrm{xx}} - \sigma_{\mathrm{yy}}}, \tag{17}$$

where β is a principal angle measured in Mohr's circle. Because the tangent function is π-periodic, satisfying $\tan 2\beta = \tan 2(\beta + \pi/2)$, two principal directions β and $\beta + \pi/2$ perpendicular to each other exist, for which Eq. (17) is fulfilled. These two principal directions, represented by β_1 and β_2 are, respectively, the principal angles of the major and minor principal stresses. By calculating β knowing the stress tensor's components' values, β will correspond to the angle from the material frame x-axis to the closest principal stress axis. For this reason, it is not possible to know from its value if the principal angle is associated with the major or minor principal stress axis. Additionally, the values of 2β range between $-90°$ and $90°$ in Mohr's circle, so that β varies between $-45°$ and $45°$ in the material frame.

Table 2. An overview of deformation's mechanical states represented through reference values of major and minor strain, major and minor stress, and stress triaxiality and Lode angle parameter, for an isotropic material and plane stress state.

Mechanical state	Major and minor strain	Major and minor stress	Stress triaxiality and Lode angle parameter
Equibiaxial compression	$\varepsilon_2/\varepsilon_1 = 1$ $\varepsilon_2 < 0$ $\varepsilon_1 < 0$	$\sigma_2/\sigma_1 = 1$ $\sigma_2 < 0$ $\sigma_1 < 0$	$\eta = -2/3$ $\bar{\theta} = 1$
Plane strain compression	$\varepsilon_2 < 0$ $\varepsilon_1 = 0$	$\sigma_2/\sigma_1 = \nu$ $\sigma_2 < 0$ $\sigma_1 < 0$	$\eta = -\sqrt{3}/3$ $\bar{\theta} = 0$
Uniaxial compression	$\varepsilon_2/\varepsilon_1 = -2$ $\varepsilon_2 < 0$ $\varepsilon_1 > 0$	$\sigma_2 < 0$ $\sigma_1 = 0$	$\eta = -1/3$ $\bar{\theta} = -1$
Shear	$\varepsilon_2/\varepsilon_1 = -1$ $\varepsilon_2 < 0$ $\varepsilon_1 > 0$	$\sigma_2/\sigma_1 = -1$ $\sigma_2 < 0$ $\sigma_1 > 0$	$\eta = 0$ $\bar{\theta} = 0$
Uniaxial tension	$\varepsilon_2/\varepsilon_1 = -0.5$ $\varepsilon_2 < 0$ $\varepsilon_1 > 0$	$\sigma_2/\sigma_1 = 0$ $\sigma_2 = 0$ $\sigma_1 > 0$	$\eta = 1/3$ $\bar{\theta} = 1$
Plane strain tension	$\varepsilon_2/\varepsilon_1 = 0$ $\varepsilon_2 = 0$ $\varepsilon_1 > 0$	$\sigma_2/\sigma_1 = \nu$ $\sigma_2 > 0$ $\sigma_1 > 0$	$\eta = \sqrt{3}/3$ $\bar{\theta} = 0$
Equibiaxial tension	$\varepsilon_2/\varepsilon_1 = 1$ $\varepsilon_2 > 0$ $\varepsilon_1 > 0$	$\sigma_2/\sigma_1 = 1$ $\sigma_2 > 0$ $\sigma_1 > 0$	$\eta = 2/3$ $\bar{\theta} = -1$

Martins et al.[18] applied this formulation presenting the principal angle related to the major principal stress axis, to show that a cruciform specimen exhibited a relatively broad distribution of the principal angle. However, this formulation ignores the case when the mechanical state is predominantly compressive in Mohr's circle, by only considering the principal angle related to the major principal stress axis; also presents different values for β depending on the shear loading direction. Moreover, the presented range of values (from $-45°$ to $135°$) is not readily associated with the tensile orientation from the rolling direction, typically evaluated between $0°$ and $90°$ for sheet metals.

Therefore, a metric based on the principal angle's formulation is proposed to evaluate the tests' sensitivity to anisotropy. It considers the maximum principal stress in absolute value, and the range of tensile orientations typically used to calibrate the material's anisotropic behaviour. This metric is named rotation angle, represented by γ, and refers to the principal direction associated with the maximum principal stress in absolute value. Its values range between $0°$ and $90°$, and is given by

$$\gamma = \begin{cases} 45 & \text{if } \sigma_{xx} = \sigma_{yy} \text{ and } \sigma_{xy} \neq 0 \\ 45(1-q) + q|\beta| & \text{otherwise} \end{cases}, \tag{18}$$

where β is the principal angle (in degrees) calculated from Eq (17), and q is an integer of value -1 or 1, calculated as

$$q = \frac{\sigma_{xx} - \sigma_{yy}}{|\sigma_{xx} - \sigma_{yy}|} \frac{|\sigma_1| - |\sigma_2|}{||\sigma_1| - |\sigma_2||}, \tag{19}$$

where $|.| = \sqrt{(.)^2}$ represents the absolute value. This formulation represents all possible states in Mohr's circle (see Fig. 6). Although each state represents different physical meanings, it is possible to mathematically reduce them to three different conditions, where the rotation angle is:

1. equal to $45°$, when $\sigma_{xx} = \sigma_{yy}$, and $\sigma_{xy} \neq 0$;
2. equal to $|\beta|$, when $\sigma_{xx} < \sigma_{yy}$ for a predominant compressive state ($|\sigma_1| < |\sigma_2|$), and when $\sigma_{xx} > \sigma_{yy}$ for a predominant tensile state ($|\sigma_1| > |\sigma_2|$), respectively, cases 1 and 2 of situations A and B (see Fig. 6); and
3. equal to $90° - |\beta|$, when $\sigma_{xx} > \sigma_{yy}$ for a predominant compressive state ($|\sigma_1| < |\sigma_2|$), and when $\sigma_{xx} < \sigma_{yy}$ for a predominant tensile state ($|\sigma_1| > |\sigma_2|$), respectively, cases 3 and 4 of situations A and B (see Fig. 6).

Numerical evaluation of heterogeneous mechanical tests

Finally, this section evaluates the heterogeneous mechanical tests, namely, Test A, Test B, Test C, and Test D. Three different materials are used in the evaluation, specifically, Cu, DP600, and AA2090-T3. The evaluation is performed using the metrics mentioned above, namely: the equivalent plastic strain; the major and minor strain; the major and minor stress; the stress triaxiality and Lode angle parameter; and the rotation angle. The results are evaluated exclusively for the increment where the FLC is reached. This simplification is made because the increment before necking occurs indicates the mechanical states observed throughout a monotonic loading test[17]. Table 3 summarises the displacements obtained at the forming limit curves of each material for every test.

Table 3. Displacements (in mm) obtained at the forming limit curves of Cu, AA2090-T3, and DP600 for Test A, Test B, Test C, and Test D.

Test	Cu	AA2090-T3	DP600
Test A	0.195	0.583	0.571
Test B	0.514	2.041	2.223
Test C	0.848	1.924	2.587
Test D	0.852	2.345	3.266

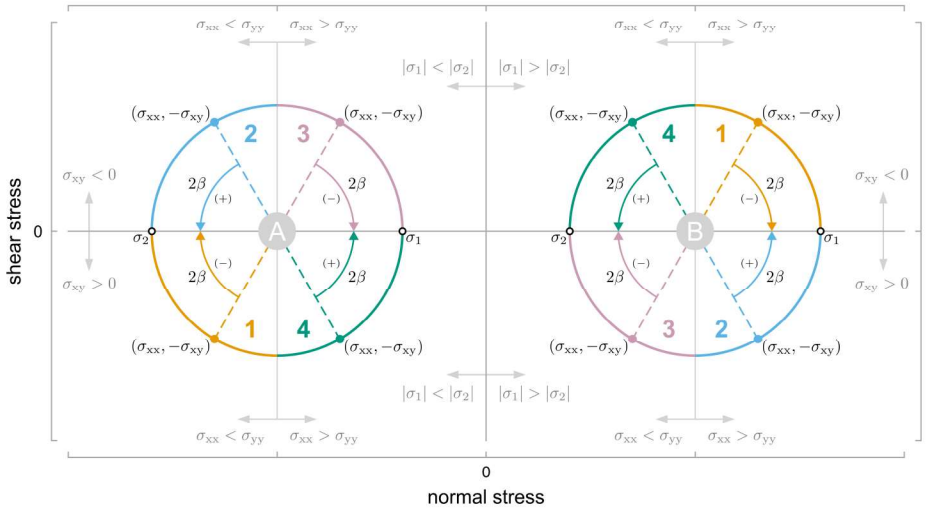

Figure 6. Schematic representation of possible states in the Mohr's circle covered by the rotation angle's formulation. Situation A is characterized by a predominant compressive state ($|\sigma_1| < |\sigma_2|$), and situation B by a predominant tensile state ($|\sigma_1| > |\sigma_2|$). Point $(\sigma_{xx}, -\sigma_{xy})$ represents the material frame section where the stresses σ_{xx} and σ_{xy} act. Cases 1, 2, 3, and 4 represent the different possibilities of calculating the principal angle 2β.

Equivalent plastic strain

The equivalent plastic strain is evaluated using the deformed contour, where the equivalent plastic strain levels are represented through a colour map (see Fig. 7). Additionally, a distinction in the representations is made between material points in elastic and plastic regimes, with the latter represented through the colour scale and the former in a single colour. This distinction between regimes enables the visualisation to focus on material points in the plastic regime, preferable, rather than material points in the elastic regime. Also, this representation provides a visual outline of the mechanical solicitation; and, as will be shown ahead, it is used to connect the metrics.

Comparing equivalent plastic strain levels between materials is not of most interest, as the observed differences are intrinsically related to the material itself. Instead, it is more interesting to analyse differences between tests for the same material. In this case, the test presenting the highest equivalent plastic strain levels is, in general, Test D, for the three materials. Concerning the equivalent plastic strain contour, the variation in the amount of material points under the plastic regime between materials is the lowest for Cu and the highest for DP600. Therefore, more mechanical information is retrieved from the latter.

An important aspect is also the homogeneity of deformation. The deformation in Test A mainly localises between adjacent arms, while most of the specimen is under low deformation levels. Test B localises the deformation in the vertically centred region, particularly in the central region and close to the free edges. Although slight differences

are observed between materials, in general, Test B presents intermediate to high levels of deformation in this region, while the rest of the specimen presents low equivalent plastic strain levels. In opposition, Test C presents two primary regions where deformation localises: at the left vertically centred region and the right curvature in the specimen's top and bottom. Low equivalent plastic strain levels are observed between these two regions, while the rest of the specimen is in the elastic regime or close to it. The distinct regions of localised deformation in Test B and Test C can be associated with different mechanical states. Lastly, Test D's deformation appears to localise at the right curvature close to the mechanical grips, and distinct regions present low to intermediate equivalent plastic strain levels, reflecting a broad diversity of mechanical states.

Major and minor strain

The major and minor strain and stress evaluations are performed through the strain- and stress-based diagrams, where circular markers coloured by equivalent plastic strain level represent material points (see Figs. 8 and 9). The diagrams have both axes normalised by an arbitrary value, to reduce the visual noise of using different axes limits. This value is specific for each material and identified in the diagram's bottom left corner.

The major and minor strain results show that the strain states mainly locate between uniaxial and plane strain tension for Test A and Test B. In the former, for AA209--T3, the strain states tend to uniaxial tension, while for DP600, it tends to plane strain tension. Although some material points with low equivalent plastic strain levels are observed in the equibiaxial tension region, it is disappointing that a biaxial test presents few material points in this region. In Test B, the two regions of high equivalent plastic strain levels are identified, particularly, for Cu and DP600 where two peaks of material points are formed. Test C and Test D present similar strain states' distributions, ranging from plane strain compression to plane strain tension. However, material points distribution in shear is denser for Test C than Test D, while the opposite observes in uniaxial compression, though with low equivalent plastic strain levels. Concerning Test C, the single peak with high equivalent plastic strain levels can suggest that the two main regions previously identified present similar strain states, therefore not providing additional mechanical information.

Major and minor stress

The first observation on the major and minor stress diagram is that material points under or close to the elastic regime, are more easily identified than in the strain-based diagram. The opposite is observed for material points under the plastic regime. Perhaps, this observation is explained by the natural shape of typical metallic sheets' stress-strain curve. The curve typically presents an accentuated slope in the elastic regime (proportional to Young's modulus), enhancing stress differences. In opposition, the curve typically presents a low slope in the plastic regime, enhancing strain differences. This observation is particularly evident for Test A, and with less expression for Test C and Test D. Concerning Test B, most material points are limited to the uniaxial tension region, presenting the lowest range of stress states from all tests. Between Test C and Test D,

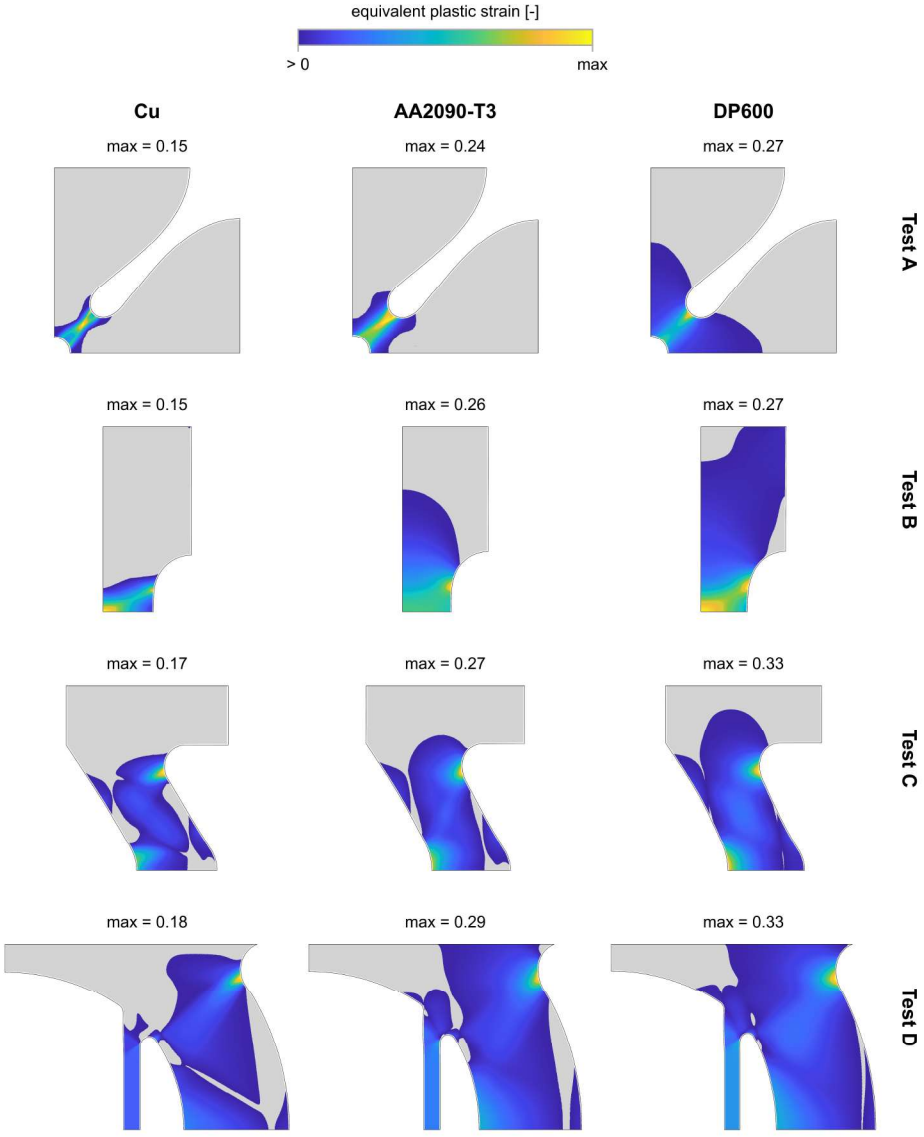

Figure 7. Equivalent plastic strain contours. Tests are represented in rows and materials in columns. Material points in the elastic and plastic regimes are distinguished, respectively, by a single colour and by the colour map. The contours are increasingly ordered by the maximum equivalent plastic strain value (shown above each contour), from left to right and from top to bottom.

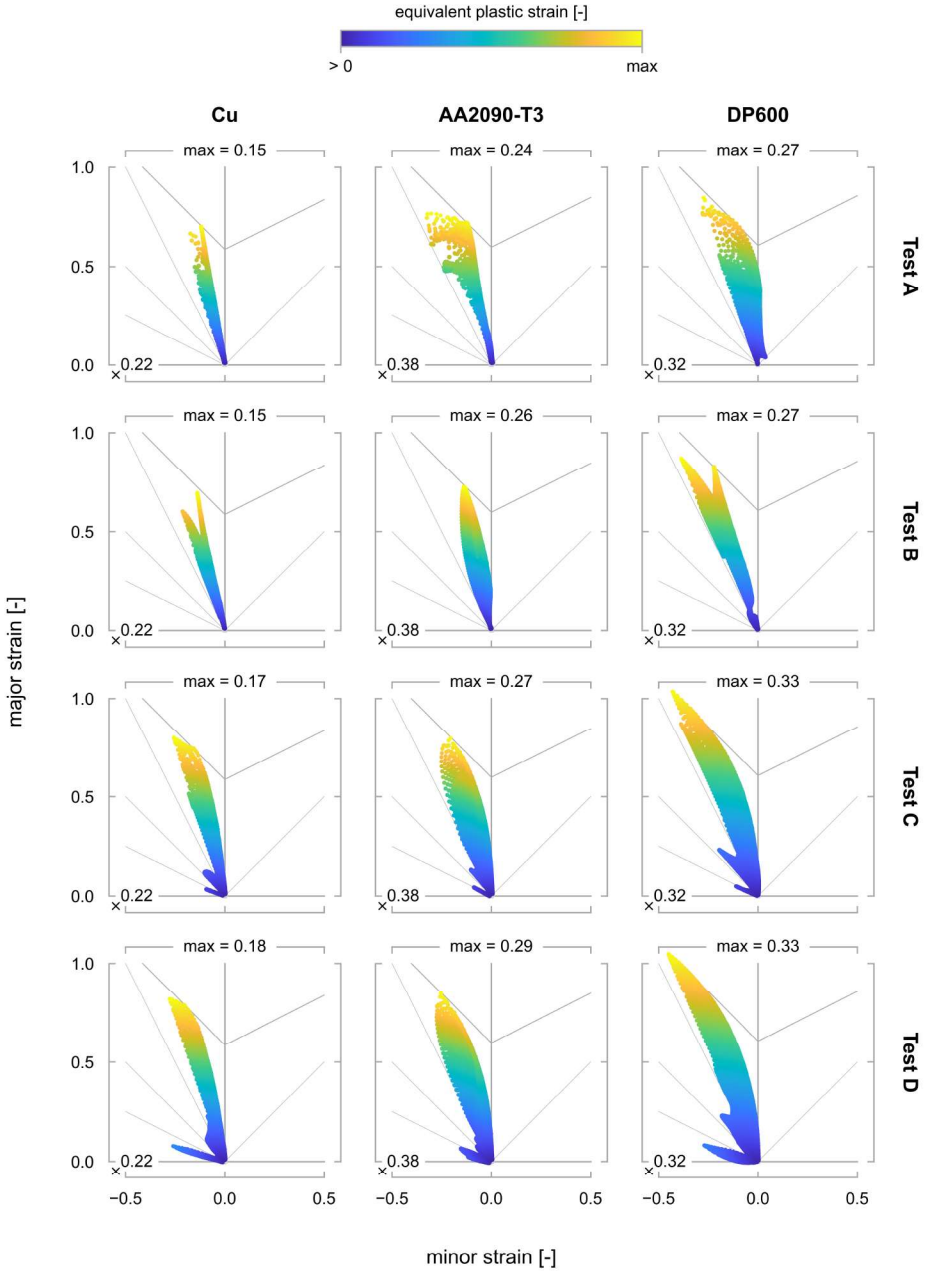

Figure 8. Major and minor strain diagrams. Tests are represented in rows and materials in columns. Material points in the elastic and plastic regimes are distinguished, respectively, by a single colour and by the colour map. The diagrams are increasingly ordered by the maximum equivalent plastic strain value (shown above each diagram), from left to right and from top to bottom. Both axes are normalized by an arbitrary value, shown in each diagram's bottom left corner.

the major and minor stress diagram is handy to accentuate differences from equibiaxial compression to shear.

Stress triaxiality and Lode angle parameter

The last metric evaluating the diversity of mechanical states is the stress triaxiality and Lode angle parameter diagram, as presented in Fig. 10. Overall, this representation appears to present less information than the two previous because only a fraction of the material points is visible, though an equal amount of information is represented. Because of the plane stress state formulation, it was expected that all the material points fall on the plane stress state curve. Even with a three-dimensional analysis, the same would be expected on a vast majority of material points, because the stress tensor's normal component can be neglected up to necking.

Test A's stress triaxiality levels indicate that all the material points are under a tensile state. For DP600, the full range of states from uniaxial to equibiaxial tension is achieved with material points in the plastic regime. On the other hand, for Cu and AA2090-T3, a higher range of stress states with high equivalent plastic strain levels is observed. Relative to Test B, Test C, and Test D, it is readily observed that these tests achieve tensile and compressive stress states. Test C lacks material points in shear, under the plastic regime, and equibiaxial to uniaxial compression. Finally, it is seen that Test D is the test achieving the highest range of stress states, from equibiaxial compression to equibiaxial tension, with material points in both regimes. In general, this diagram replicates the major and minor stress diagram through a different stress tensor representation. While the former represents the decomposition of the hydrostatic and deviatoric stress contributions, the latter stands for the principal values. Nonetheless, this metric can complement the previous two, providing an instant understanding of the stress states achieved.

Rotation angle

Finally, the rotation angle's results are presented in Fig. 11 through a histogram of area densities. The histogram divides the rotation angle entire range of values into 90 equal intervals, representing the specimen's area proportional amount. Using the area density minimises the finite element mesh's influence in the results. Each interval is also discretised by equivalent plastic strain levels, similar to the previous metrics' materials points.

Test A presents material points in the full range of rotation angle (elastic and plastic regimes), indicating a good sensitivity of the test to anisotropy. However, material points presenting high equivalent plastic strain levels locate only between $30°$ and $60°$. It can be noticed that the rotation angle distribution is centred close to $0°$ for Test B, Test C and Test D, which is related to the orientation of the loading direction with respect to the material orientation. When changing the material orientation, mainly a shift of the distribution is noticed, but also some spreading of the distribution, especially at $45°$. Test B presents the least range of values for all materials, exclusively from $0°$ to $45°$, and most material points locate between $0°$ and $15°$, indicating low sensitivity to anisotropy. Specifically, for Cu, the density of material points presenting rotation angle levels higher

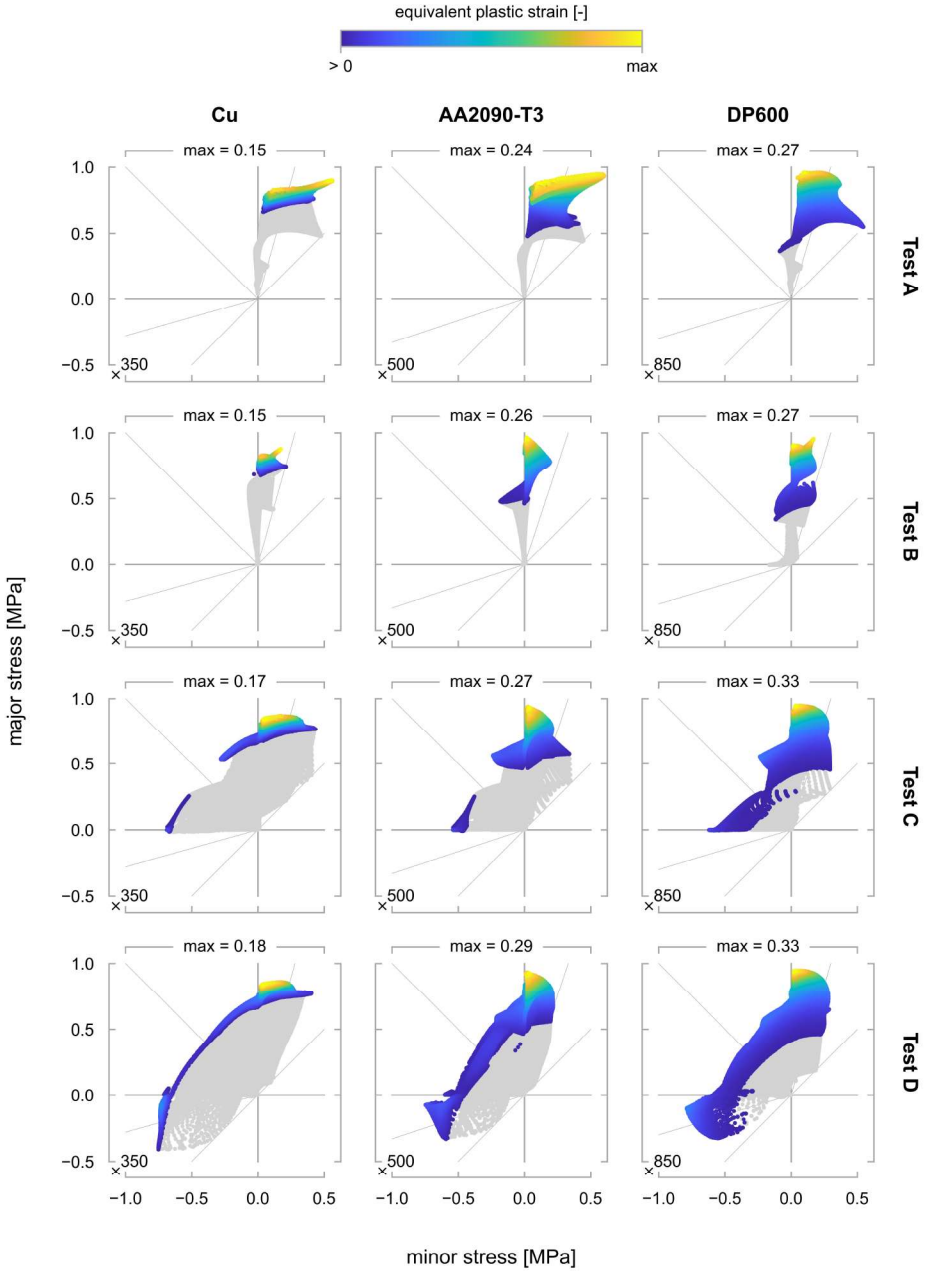

Figure 9. Major and minor stress diagrams. Tests are represented in rows and materials in columns. Material points in the elastic and plastic regimes are distinguished, respectively, by a single colour and by the colour map. The diagrams are increasingly ordered by the maximum equivalent plastic strain value (shown above each diagram), from left to right and from top to bottom. Both axes are normalized by an arbitrary value, shown in each diagram's bottom left corner.

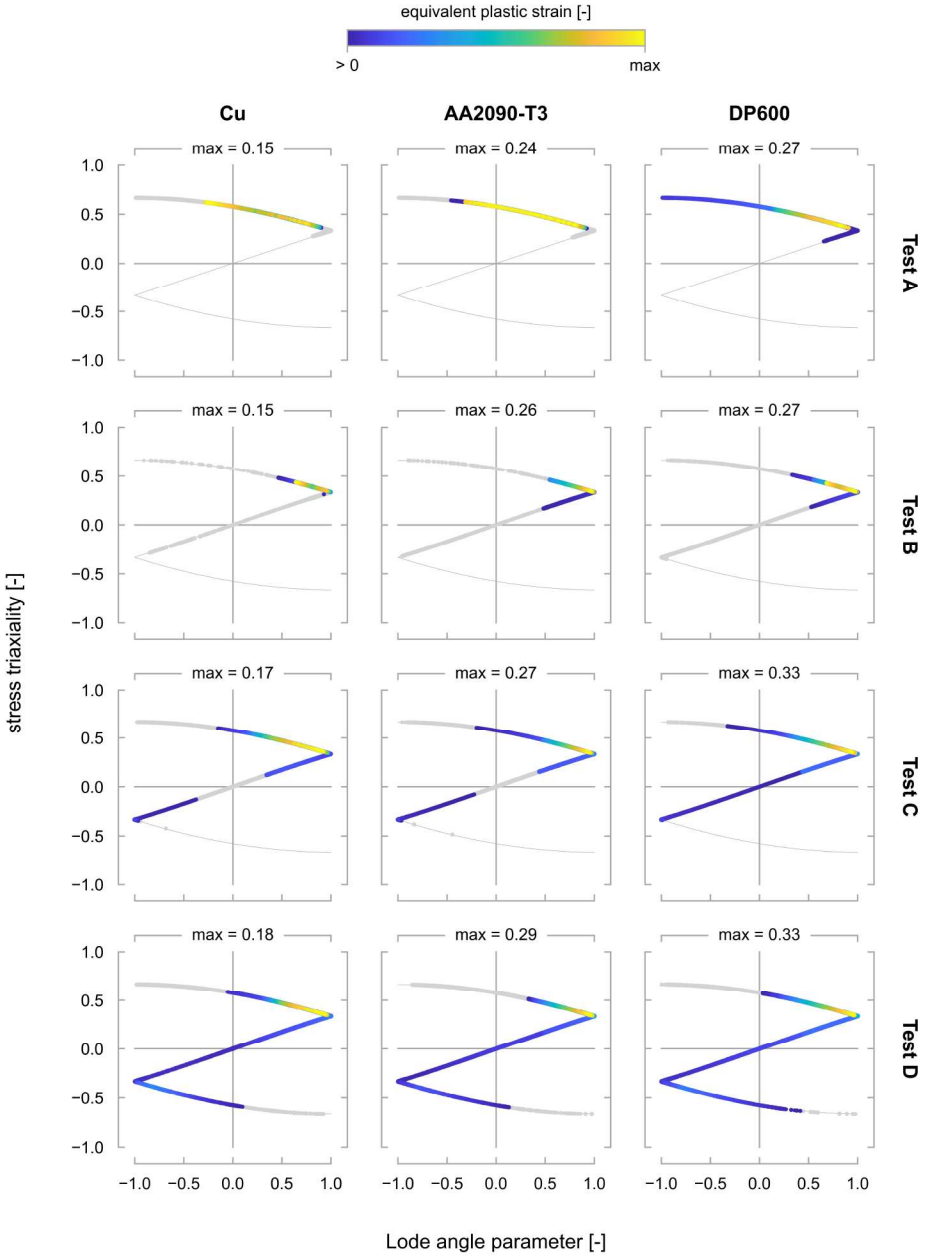

Figure 10. Stress triaxiality and Lode angle parameter diagrams. Tests are represented in rows and materials in columns. Material points in the elastic and plastic regimes are distinguished, respectively, by a single colour and by the colour map. All the material points are located on top of the plane stress curve. The diagrams are increasingly ordered by the maximum equivalent plastic strain value (shown above each diagram), from left to right and from top to bottom.

than $15°$ is low, and the existing present low equivalent plastic strain levels. On a positive note, for AA2090-T3 and DP600, the density of material points with rotation angle values higher than $15°$ tends to increase. Both Test C and Test D achieve the full range of rotation angle values; however, from $45°$ to $90°$, the material points are in the elastic regime or close to it. The ability to cover a high range of values means that the density of values will be more evenly distributed. Particularly for Test C, this remark reflects the good density of material points in the histogram's central region and the overall low-density values (lower than 5%).

Nonetheless, most material points in Test C locate close to $0°$, but material points with high equivalent plastic strain levels are observed up to $30°$. In Test D, the rotation angle's distribution is not as even as in Test C, because the histogram's first interval (0–$1°$) aggregates more than 10% of the specimen's total area. Even so, the density and equivalent plastic strain levels of material points between $0°$ and $30°$ are in the same order of Test C. Ultimately, Test A is the one that presents the highest range of rotation angle levels for material points in the plastic regime. Therefore, it can be considered the most sensitive test to anisotropy. However, as Test A is a biaxial loading test, it is naturally advantageous relative to the other tests. Test C presents the evenest distribution out of the latter while achieving values up to $45°$ under the plastic regime.

From a global perspective, it appears that these tests individually cannot fully characterise the material's strain-hardening and anisotropic behaviour. Nonetheless, Test D could better characterise the strain-hardening than the other tests, due to higher equivalent plastic strain levels and diversity of mechanical states. However, Test B presents a more homogeneous distribution of deformation and can also be regarded as a suitable choice for the strain-hardening characterisation, even if the range of mechanical states is reduced. Regarding the materials' anisotropic behaviour, the rotation angle suggests that Test A can better characterise this behaviour. However, this test requires a nonstandard testing machine, in contrast to the other tests, which can be performed on a universal testing machine. Given the possibility of performing two tests, the combination of different tensile orientations, such as, at $0°$ and $90°$, of Test D or Test C can increase the anisotropic information observed in the rotation angle.

Conclusion

In this work, the richness of heterogeneous mechanical tests is evaluated using five metrics. The analysis considers four heterogeneous mechanical tests and three virtual materials, providing additional validation of each test's potential and demonstrating the relevance of evaluating tests for different materials.

The performed evaluation shows that the equivalent plastic strain is relevant to evaluate the levels of strain achieved and deformation's homogeneity. The mechanical states' diversity is evaluated using the major and minor strain, the major and minor stress, and the stress triaxiality and Lode angle parameter. Even though these metrics represent the strain and stress tensors, each one presents characteristics that complement each other. However, the simultaneous use of the three can be considered excessive. To avoid redundant representations, the use of the major and minor strain should be a priority,

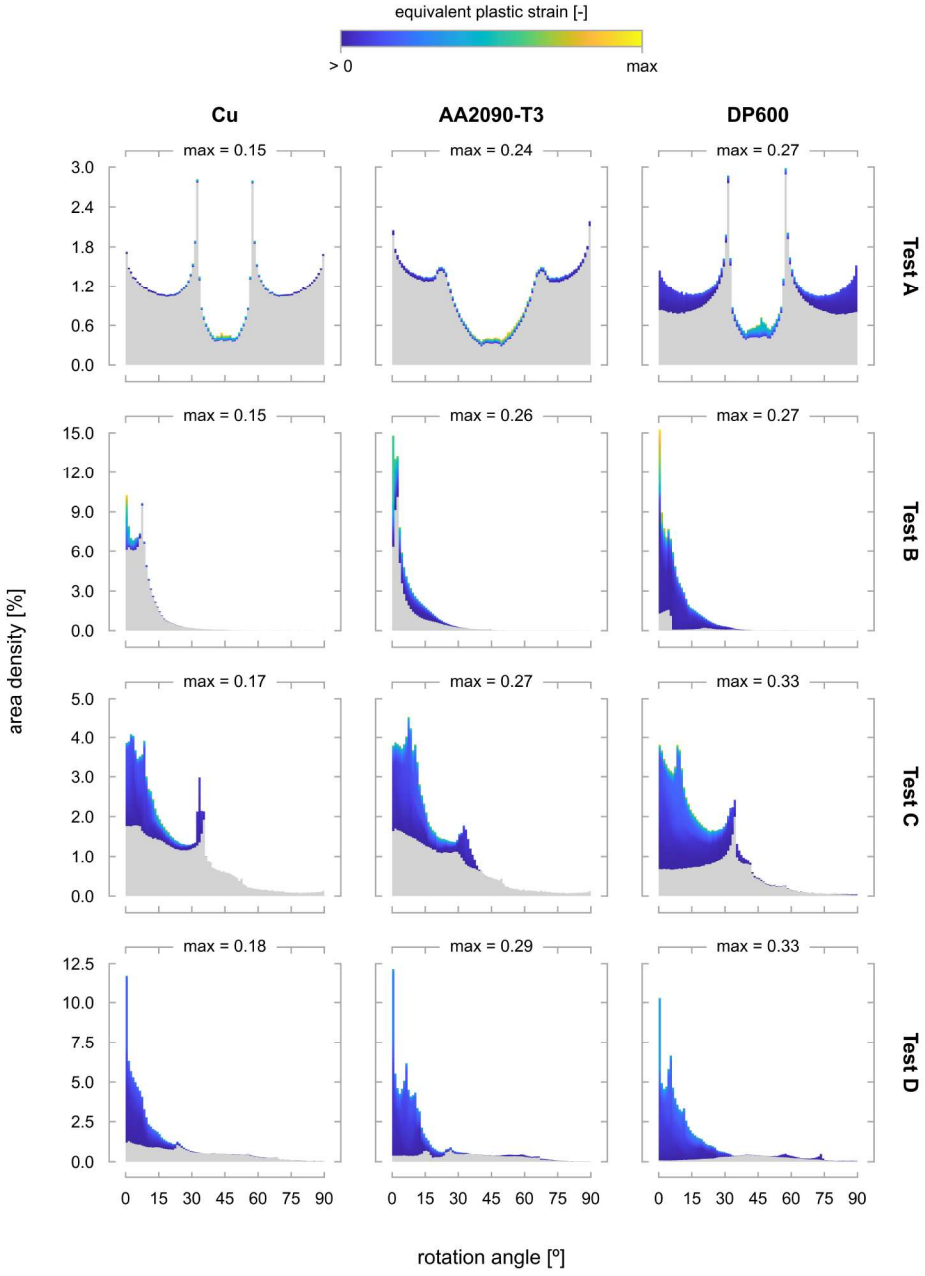

Figure 11. Rotation angle histograms. Tests are represented in rows and materials in columns. The rotation angle's range of values $(0–90°)$ is divided into 90 equal intervals. Material points in the elastic and plastic regimes are distinguished, respectively, by a single colour and by the colour map. The histograms are increasingly ordered by the maximum equivalent plastic strain value (shown above each histogram), from left to right and from top to bottom.

because it can be experimentally measured. Additionally, the major and minor stress is an excellent complement to the major and minor strain and should be used whenever possible. In opposition, the use of the stress triaxiality and Lode angle parameter can be regarded as optional, since the amount of visible information is lower than in the other two. Lastly, the rotation angle is proposed to evaluate the tests' sensitivity to anisotropy. Through its use, it is possible to assess the range of material orientations achieved. It is expected that this metric can be useful to evaluate the potential of heterogeneous mechanical tests to calibrate the material's anisotropic behaviour.

A test achieving a high range of mechanical states, from equibiaxial compression to equibiaxial tension, was identified. Moreover, the biaxial loading test leads to the lowest equivalent plastic strain levels, but is also the most sensitive test to anisotropy. Nonetheless, two uniaxial loading tests also show great potential to characterise the material's anisotropic behaviour, if two tests of different tensile orientations are combined.

In summary, this work provides a basis to evaluate heterogeneous mechanical tests using various metrics. Hopefully, it can contribute to the development of heterogeneous mechanical tests by considering the materials' anisotropic behaviour and providing a basis to evaluate their richness. Future work should validate these findings by inversely identifying the considered material parameters using the heterogeneous mechanical tests.

Declaration of conflicting interests

The authors declared no potential conflicts of interest with respect to the research, authorship, and/or publication of this article.

Funding

This project has received funding from the Research Fund for Coal and Steel under grant agreement No 888153. The authors also gratefully acknowledge the financial support of the Portuguese Foundation for Science and Technology (FCT) under the projects PTDC/EME-APL/29713/2017, PTDC/EME-EME/31243/2017 and PTDC/EME-EME/30592/2017 by UE/FEDER through the programs CENTRO 2020 and COMPETE 2020, and UID/EMS/00481/2013-FCT under CENTRO-01-0145-FEDER-022083. The authors also would like to acknowledge the Région Bretagne for its financial support and BPI France under project EXPRESSo. M.G. Oliveira is grateful to the FCT for the PhD grant SFRH/BD/143665/2019.

References

1. Souto N, Andrade-Campos A and Thuillier S. Material parameter identification within an integrated methodology considering anisotropy, hardening and rupture. *Journal of Materials Processing Technology* 2015; 220: 157–172. DOI:10.1016/j.jmatprotec.2015.01.017.
2. Barlat F, Aretz H, Yoon JH et al. Linear transfomation-based anisotropic yield functions. *International Journal of Plasticity* 2005; 21(5): 1009–1039. DOI:10.1016/j.ijplas.2004.06.004.

3. Cazacu O, Plunkett B and Barlat F. Orthotropic yield criterion for hexagonal closed packed metals. *International Journal of Plasticity* 2006; 22(7): 1171–1194. DOI:10.1016/j.ijplas.2005.06.001.
4. Haddadi H and Belhabib S. Improving the characterization of a hardening law using digital image correlation over an enhanced heterogeneous tensile test. *International Journal of Mechanical Sciences* 2012; 62(1): 47–56. DOI:10.1016/j.ijmecsci.2012.05.012.
5. International Digital Image Correlation Society, Jones EMC and Iadicola MA (Eds). *A good practices guide for digital image correlation*. 2018. DOI:10.32720/idics/gpg.ed1.
6. Grédiac M, Blaysat B and Sur F. On the optimal pattern for displacement field measurement: Random speckle and DIC, or checkerboard and LSA? *Experimental Mechanics* 2020; : 1–26DOI:10.1007/s11340-019-00579-z.
7. Pierron F. Test design for identification from full-field measurements: A consise review. In *Residual Stress, Thermomechanics & Infrared Imaging and Inverse Problems*, volume 6. Springer International Publishing. ISBN 9783030300975, pp. 105–110. DOI:10.1007/978-3-030-30098-2_16.
8. Blaysat B, Neggers J, Grédiac M et al. Towards criteria characterizing the metrological performance of full-field measurement techniques: Application to the comparison between local and global versions of DIC. *Experimental Mechanics* 2020; 60(3): 393–407. DOI:10.1007/s11340-019-00566-4.
9. Prates P, Pereira A, Sakharova N et al. Inverse strategies for identifying the parameters of constitutive laws of metal sheets. *Advances in Materials Science and Engineering* 2016; 2016: 1–18. DOI:10.1155/2016/4152963.
10. Aquino J, Andrade-Campos A, Martins J et al. Design of heterogeneous mechanical tests: Numerical methodology and experimental validation. *Strain* 2019; 55(4). DOI:10.1111/str.12313.
11. Grédiac M, Pierron F, Avril S et al. The virtual fields method for extracting constitutive parameters from full-field measurements: a review. *Strain* 2006; 42(4): 233–253. DOI:10.1111/j.1475-1305.2006.tb01504.x.
12. Pierron F and Grédiac M. *The virtual fields method*. New York, NY: Springer-Verlag New York, 2012. ISBN 9781461418238. DOI:10.1007/978-1-4614-1824-5.
13. Souto N, Andrade-Campos A and Thuillier S. A numerical methodology to design heterogeneous mechanical tests. *International Journal of Mechanical Sciences* 2016; 107: 264–276. DOI:10.1016/j.ijmecsci.2016.01.021.
14. Souto N, Andrade-Campos A and Thuillier S. Mechanical design of a heterogeneous test for material parameters identification. *International Journal of Material Forming* 2017; 10(3): 353–367. DOI:10.1007/s12289-016-1284-9.
15. Rossi M, Badaloni M, Lava P et al. A procedure for specimen optimization applied to material testing in plasticity with the virtual fields method. *AIP Conference Proceedings* 2016; 1769(1): 200016. DOI:10.1063/1.4963634.
16. Fu J, Xie W, Zhou J et al. A method for the simultaneous identification of anisotropic yield and hardening constitutive parameters for sheet metal forming. *International Journal of Mechanical Sciences* 2020; 181: 105756. DOI:10.1016/j.ijmecsci.2020.105756.
17. Souto N, Thuillier S and Andrade-Campos A. Design of an indicator to characterize and classify mechanical tests for sheet metals. *International Journal of Mechanical Sciences* 2015;

101-102: 252–271. DOI:10.1016/j.ijmecsci.2015.07.026.
18. Martins J, Andrade-Campos A and Thuillier S. Calibration of anisotropic plasticity models using a biaxial test and the virtual fields method. *International Journal of Solids and Structures* 2019; 172-173(1): 21–37. DOI:10.1016/j.ijsolstr.2019.05.019.
19. Hapsari G, Richard F, Hmida RB et al. Instrumented incremental sheet testing for material behavior extraction under very large strain: Information richness of continuous force measurement. *Materials & Design* 2018; 140: 317–331. DOI:10.1016/j.matdes.2017.12.002.
20. Barlat F, Brem J, Yoon JH et al. Plane stress yield function for aluminum alloy sheets—part 1: theory. *International Journal of Plasticity* 2003; 19(9): 1297–1319. DOI:10.1016/s0749-6419(02)00019-0.
21. Yoon J, Barlat F, Dick R et al. Prediction of six or eight ears in a drawn cup based on a new anisotropic yield function. *International Journal of Plasticity* 2006; 22(1): 174–193. DOI:10.1016/j.ijplas.2005.03.013.
22. Abedini A, Butcher C, Rahmaan T et al. Evaluation and calibration of anisotropic yield criteria in shear loading: Constraints to eliminate numerical artefacts. *International Journal of Solids and Structures* 2018; 151: 118–134. DOI:10.1016/j.ijsolstr.2017.06.029.
23. Comsa D, Paraianu L, Bichis I et al. A new formulation of the MMFC to avoid the numerical instability. In *Proceedings of 4th Forming Technology Forum 2011*. Zurich, Switzerland: ETH Zurich, Institute of Virtual Manufacturing.
24. Ozturk F, Toros S and Kilic S. Effects of anisotropic yield functions on prediction of forming limit diagrams of DP600 advanced high strength Steel. *Procedia Engineering* 2014; 81: 760–765. DOI:10.1016/j.proeng.2014.10.073.
25. Pham C, Thuillier S and Manach P. Experimental and numerical investigation of the formability of an ultra-thin copper sheet. *Journal of Physics: Conference Series* 2017; 896(1): 012109. DOI:10.1088/1742-6596/896/1/012109.
26. Thuillier S, Pham C and Manach P. 2D springback and twisting after drawing of copper alloy sheets. *Journal of Physics: Conference Series* 2018; 1063(1): 012124. DOI:10.1088/1742-6596/1063/1/012124.
27. Zhang R, Shao Z and Lin J. A review on modelling techniques for formability prediction of sheet metal forming. *International Journal of Lightweight Materials and Manufacture* 2018; 1(3): 115–125. DOI:10.1016/j.ijlmm.2018.06.003.
28. Paul S. Theoretical analysis of strain- and stress-based forming limit diagrams. *The Journal of Strain Analysis for Engineering Design* 2013; 48(3): 177–188. DOI:10.1177/0309324712468524.
29. Schmaltz S and Willner K. Comparison of different biaxial tests for the inverse identification of sheet steel material parameters. *Strain* 2014; 50(5): 389–403. DOI:10.1111/str.12080.
30. Belhabib S, Haddadi H, Gaspérini M et al. Heterogeneous tensile test on elastoplastic metallic sheets: Comparison between FEM simulations and full-field strain measurements. *International Journal of Mechanical Sciences* 2008; 50(1): 14–21. DOI:10.1016/j.ijmecsci.2007.05.009.
31. Kim JH, Barlat F, Pierron F et al. Determination of anisotropic plastic constitutive parameters using the virtual fields method. *Experimental Mechanics* 2014; 54(7): 1189–1204. DOI:10.1007/s11340-014-9879-x.

32. Jones E, Carroll J, Karlson K et al. Parameter covariance and non-uniqueness in material model calibration using the virtual fields method. *Computational Materials Science* 2018; 152(Exp. Mech. 48 4 2008): 268–290. DOI:10.1016/j.commatsci.2018.05.037.
33. Takizawa H, Oide K, Suzuki K et al. Development of the user subroutine library "Unified Material Model Driver for Plasticity (UMMDp)" for various anisotropic yield functions. *Journal of Physics: Conference Series* 2018; 1063(1): 012099. DOI:10.1088/1742-6596/1063/1/012099.
34. Cooreman S, Lecompte D, Sol H et al. Identification of mechanical material behavior through inverse modeling and DIC. *Experimental Mechanics* 2008; 48(4): 421–433. DOI: 10.1007/s11340-007-9094-0.
35. Avril S, Pierron F, Pannier Y et al. Stress reconstruction and constitutive parameter identification in plane-stress elasto-plastic problems using surface measurements of deformation fields. *Experimental Mechanics* 2008; 48(4): 403–419. DOI:10.1007/s11340-007-9084-2.
36. Rossi M, Pierron F and Štamborská M. Application of the virtual fields method to large strain anisotropic plasticity. *International Journal of Solids and Structures* 2016; 97: 322–335. DOI: 10.1016/j.ijsolstr.2016.07.015.
37. Barroqueiro B, Andrade-Campos A, Dias-de Oliveira J et al. Design of mechanical heterogeneous specimens using topology optimization. *International Journal of Mechanical Sciences* 2020; 181: 105764. DOI:10.1016/j.ijmecsci.2020.105764.
38. Bai Y and Wierzbicki T. A new model of metal plasticity and fracture with pressure and Lode dependence. *International Journal of Plasticity* 2008; 24(6): 1071–1096. DOI: 10.1016/j.ijplas.2007.09.004.
39. Danas K and Castañeda PP. Influence of the Lode parameter and the stress triaxiality on the failure of elasto-plastic porous materials. *International Journal of Solids and Structures* 2012; 49(11-12): 1325–1342. DOI:10.1016/j.ijsolstr.2012.02.006.
40. Kiran R and Khandelwal K. A triaxiality and Lode parameter dependent ductile fracture criterion. *Engineering Fracture Mechanics* 2014; 128: 121–138. DOI:10.1016/j.engfracmech.2014.07.010.